

## Design and simulation of a refractive index sensor based on SPR and LSPR using gold nanostructures



Armin Agharazy Dormeny\*, Parsoua Abedini Sohi, Mojtaba Kahrizi

Department of Electrical and Computer Engineering, Concordia University, Montreal H3G 1M8, Canada

### ARTICLE INFO

#### Keywords:

Surface plasmon  
Sensor  
COMSOL multiphysics  
LSPR  
Nanowire arrays  
Nanohole arrays

### ABSTRACT

A refractive index sensor to detect chemicals based on surface plasmon resonance is designed and analytically investigated by a finite element method via COMSOL multiphysics. A tunable sensitivity is achieved by patterning the continuous metallic thin films with cavities or protrusions. The simulation results exhibit that the improved sensitivity of the devices is attributed to the co-excitation of SPR and LSPR modes. This result is obtained by studying the variation of the electric field intensity along several cut lines through the metallic layer. The penetration depth of the plasmon field is characterized, and accordingly, SPR and LSPR modes of the sensors are determined. The proposed sensor is calibrated for eight substances with refractive indices ranging from 1.333 to 1.38. The linearity of the calibration curve indicates the applicability of the sensor to identify the refractive indices of unknown mediums as a function of resonance wavelength. This study is proposing a new way to show the duality nature of patterned thin films to support both propagating and localized surface plasmon modes.

### Introduction

Surface plasmon resonance (SPR) is the collective resonance of conduction electrons, stimulated by light. Oscillation of electrons occurs at the interface between negative and positive permittivity materials, i.e., metal and a dielectric material [1]. SPR phenomenon is observed by various techniques such as Kretschmann [2], and Otto [3] configurations, and metal-coated fiber optic [4]. These configurations have been appropriately used to develop high sensitive sensors for highly versatile applications such as chemical/biological sensing [5,6], gas sensors [7], and clinical diagnostics [8].

The changes in the refractive index of the surrounding medium affect the resonance condition, which can be experimentally observed as a change in the absorption spectrum. The changes could be the resonance wavelength, the absorption peak strength and the full width half maximum (FWHM) of the absorption spectrum. Sensitivity and figure of merit (FOM) are the parameters used to define the performance of the SPR sensors [9,10], which could be tuned by applying patterned thin films or metallic nanostructures [11–14]. Beside the enhancement of electric fields using SPR and LSPR, other approaches utilizing metamaterials to enhance magnetic plasmon resonance are reported [15–17]. Various strategies such as Fabry-Perot cavities are investigated [18–20] to improve the sensitivity and narrowing the linewidth of the refractive index sensors.

In common SPR sensors, metallic thin film/prism structure induces a propagating surface plasmon resonance (PSPR). Applying metallic nanostructures rather than using thin films results in generating localized surface plasmon resonance (LSPR) which is more sensitive to local refractive index surrounding the nanostructures, it is often used to detect molecular absorption on the surface of a material. LSPR results in non-propagating surface plasmon resonance as the excitation is confined to the volume of nanoparticles with a size much smaller than the photon wavelength [21].

Utilizing complex nanostructures that benefit from the combination of localized and delocalized surface plasmons (SPs) (such as micro/nano-patterned thin films) can enhance the device performance. The sensitivity of the device can be tuned by changing the periodicity, size, and shape of the structures [22,23].

In this work, 3D modeling and simulation of devices based on SPR is investigated using COMSOL Multiphysics (optics module). In this model, the ability to tailor the geometrical properties of nanostructures provides a realistic study to improve the performance of SPR/LSPR based sensors. The effect of various metallic layer configurations such as planar, perforated, and protrusive thin films on the sensitivity and accuracy of the sensors are studied. The enhancement of the electric field around the structures, the decay length of the electric field at the metal-dielectric interface and the performance of the sensors for each configuration are analytically investigated and reported. For the first

\* Corresponding author.

E-mail address: [a\\_ghar@encs.concordia.ca](mailto:a_ghar@encs.concordia.ca) (A. Agharazy Dormeny).

<https://doi.org/10.1016/j.rinp.2019.102869>

Received 4 November 2019; Received in revised form 6 December 2019; Accepted 7 December 2019

Available online 10 December 2019

2211-3797/ © 2019 The Authors. Published by Elsevier B.V. This is an open access article under the CC BY-NC-ND license (<http://creativecommons.org/licenses/by-nc-nd/4.0/>).

time, the study of variation of the electric field along various cut lines through the thin film analytically confirms the co-excitation of SPR and LSPR simultaneously. As experimental results of SPR in the planar thin film are frequently reported in the literature, the results of the thin film study are verified accordingly.

### Device modeling and simulation setup

The wave optics module of COMSOL Multiphysics is used to design and simulate a refractive index sensor based on SPR. The device consists of a silica glass layer with a permittivity ( $\epsilon_s$ ) defined as a function of incident light wavelength ( $\lambda$ ,  $\mu\text{m}$ )

$$\epsilon_s = 1 + \frac{a_1\lambda^2}{\lambda^2 - b_1^2} + \frac{a_2\lambda^2}{\lambda^2 - b_2^2} + \frac{a_3\lambda^2}{\lambda^2 - b_3^2} \quad (1)$$

where  $a_1 = 0.696749$ ,  $a_2 = 0.408218$ ,  $a_3 = 0.890815$ ,  $b_1 = 0.0690660$  ( $\mu\text{m}$ ),  $b_2 = 0.115662$  ( $\mu\text{m}$ ),  $b_3 = 9.900559$  ( $\mu\text{m}$ ) [24]. The silica glass layer is coated with a gold thin film (with various configurations) at the vicinity of the sensing medium with a known refractive index. The experimental data of gold refractive index as a function of wavelength is imposed as a COMSOL interpolation function [25]. For appropriate meshing, the maximum and minimum element sizes were set to 5 nm and 1 nm, respectively.

Fig. 1 shows the geometrical configuration of the modeled device. As it is shown in the figure, Floquet periodic boundary condition (FPBC) was imposed on all plane boundaries along the z-axis of the structure to satisfy the “semi-infinite” condition for the excitation of SPs. This condition assumes that the model is infinitely large, and the designed unit cell is repeating periodically in the plane of the gold thin film. On periodic boundaries, the electric field component of the light is defined as [26]

$$E = e^{-jk_F \cdot r} \quad (2)$$

where  $r$  is a vector perpendicular to the symmetry boundaries, and its magnitude is proportional to the distance between the symmetry boundaries which is automatically defined by the software. The x and y components of the wave vector  $k_F$  is defined as

$$k_F = \{k_{Fx}, k_{Fy}\} = \left\{ \frac{2\pi}{\lambda} \sqrt{\epsilon} \cos\theta, \frac{2\pi}{\lambda} \sqrt{\epsilon} \sin\theta \right\} \quad (3)$$

where  $\theta$  is the angle between the incident light and the x-y plane, and  $\epsilon$  is the permittivity of the periodic mediums.

At resonance condition, the wave vector of the incident light matches the wave vector of the electrons oscillating on the metal surface [27]. Hence to excite SPs, it is required to have the components of the electric field acting along the metal-dielectric interface. Therefore, SPs are only excited by p-polarized incident light. P-polarized incident

light, which refers to as transverse-magnetic wave ( $H_{TM}$ ) at port 1, is defined as

$$H_{TM} = \left\{ 0, e^{-j\left(\frac{2\pi}{\lambda} \sqrt{\epsilon_S} \cos\theta \cdot x + \frac{2\pi}{\lambda} \sqrt{\epsilon_S} \sin\theta \cdot z\right)}, 0 \right\} \quad (4)$$

in which the terms  $\epsilon_s$ ,  $\lambda$  and  $\theta$  are the same as defined in Eqs. (1) and (3).

### Results and discussion

#### SPR in planar thin films

To investigate the effect of the metallic layer thickness on the device performance, thin films with thicknesses of 20, 40, 60 and 80 nm were considered in the structures of four different sensors. For each device, the absorption spectrum with wavelengths ranging from 300 to 850 nm was measured to detect glycerol with a refractive index of 1.357.

The absorption data of the devices are shown in Fig. 2a. The observations demonstrate two distinct regions in the spectrum, inter-band (IB) and SPR. IB absorption spectra (near-UV) are due to the excitation of the electrons from lower shells of the gold atom to the conduction band by the incident light. The position of the peaks in this region is independent of the thickness and configuration of the thin films [28], and they were observable as we used the experimental data of gold refractive index in our model [29].

In the SPR region of Fig. 2a, consistent with what reported in the literature [30,31], increasing the gold thickness induces a red-shift in the resonance wavelength. Among the devices, the one with 40 nm gold layer showed the highest absorption peak at the wavelength of 656 nm. Also, the device showed the best resolution (smallest FWHM) compared to other devices. As the thickness of the thin film is increased above 40 nm, the absorption spectrum is broadened, and its peak is lowered significantly.

The sensitivity of the sensor,  $S_n$ , is defined as

$$S_n \left( \frac{\text{nm}}{\text{RIU}} \right) = \frac{\delta\lambda_{\text{res}}}{\delta n_d} \quad (5)$$

where  $\delta\lambda_{\text{res}}$  is the offset of the resonance peak and  $\delta n_d$  is the change in the refractive index of the dielectric medium [32].

To compare the sensitivities of the sensors, the absorption spectra of models made of thin films with 20, 40 and 60 nm thicknesses were obtained for dielectric materials glycerol with a refractive of 1.357 (shown by solid lines in Fig. 2b) and pure water (shown by dotted lines in Fig. 2b) with a refractive index of 1.333. The change in the position of the resonance peaks versus the refractive index of the surrounding fluid is also shown in Fig. 2b. As one can observe, the resonance wavelength has a red-shift in all devices when the refractive index of the medium is increased. The red-shift of the resonance wavelength caused by the 60 nm thin film is the largest among the studied devices, and it is equal to  $1833 \frac{\text{nm}}{\text{RIU}}$  compared to  $1666 \frac{\text{nm}}{\text{RIU}}$  and  $833 \frac{\text{nm}}{\text{RIU}}$  for the devices modeled with 40 and 20 nm thin films, respectively.

Although the sensitivity of 60 nm-model was slightly higher than that of 40 nm-device, the latter showed higher accuracy due to its lower FWHM. Therefore, the 40 nm-model was chosen for further studies. The effect of the patterned thin film and their configurations are explored in the following sections.

The spatial extension of the electric field associated with resonance wavelength for the model made of 40 nm film is shown in Fig. 2c. Theoretically, the exponential decay of the electric field in both sides of the metal-dielectric interface confirms that the observed absorbance peak is due to the SPR phenomenon. The decay length of 204 nm is observed for this sensor. This value is defined as the distance, in which the electric field strength reduces to %37 of the peak amplitude at the metal-dielectric interface [33].

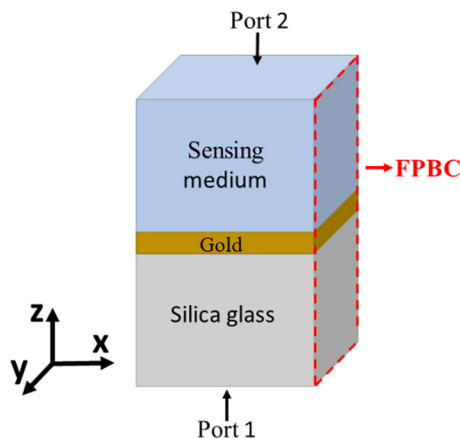
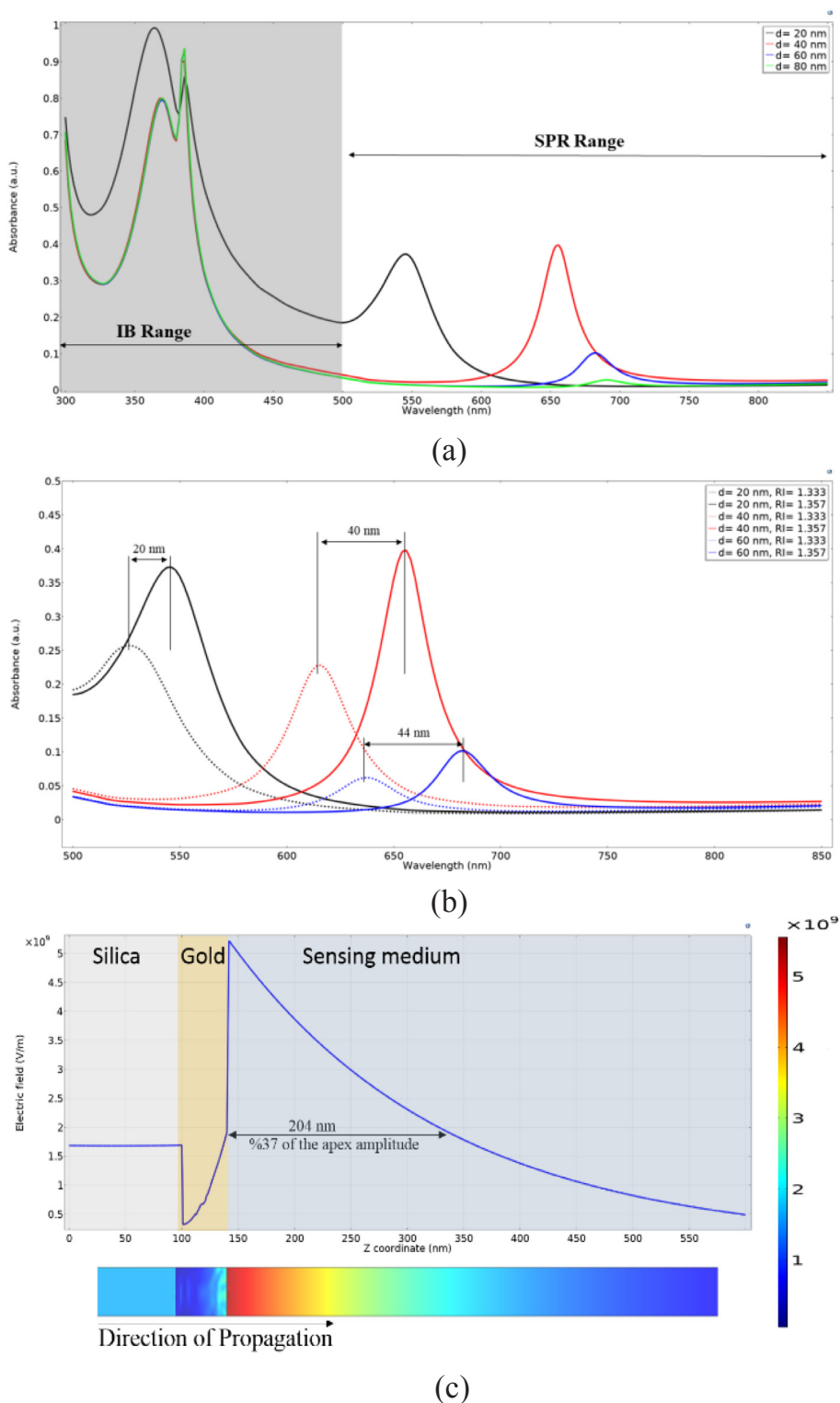


Fig. 1. 3D geometry of the designed unit cell with dimensions of  $20 \text{ nm} \times 20 \text{ nm} \times 2 \mu\text{m}$ . FPBC is imposed on all vertical faces of the cell.



**Fig. 2.** (a) The absorbance spectra of the designed devices with gold thin film thicknesses of, 20, 40, 60 and 80 nm for detecting glycerol as the sensing medium ( $n = 1.357$ ). (b) The red-shift of the resonance wavelength of the sensors made of 20, 40 and 60 nm thin film of gold as the refractive index of the medium is increased from 1.333 (dotted lines) to 1.357 (solid lines). (c) SPR decay length of 204 nm toward the dielectric region for the 40 nm thin film sensor (color legend shows the distribution of electric field in  $\frac{V}{m}$  unit). (For interpretation of the references to color in this figure legend, the reader is referred to the web version of this article.)

*Nanovoid and nanohole patterned thin films*

To study the SPR in thin films patterned with periodic structures, a gold layer with a thickness of 40 nm perforated with arrays of

cylindrical cavities is modeled. In this model, the diameter of the cavities is considered 10 nm and the effect of the depth of the cavities is investigated for four values of 10, 20, 30 and 40 nm. Hereafter, “nanovoid” is referred to shallow cavities (with a depth of 10, 20 and

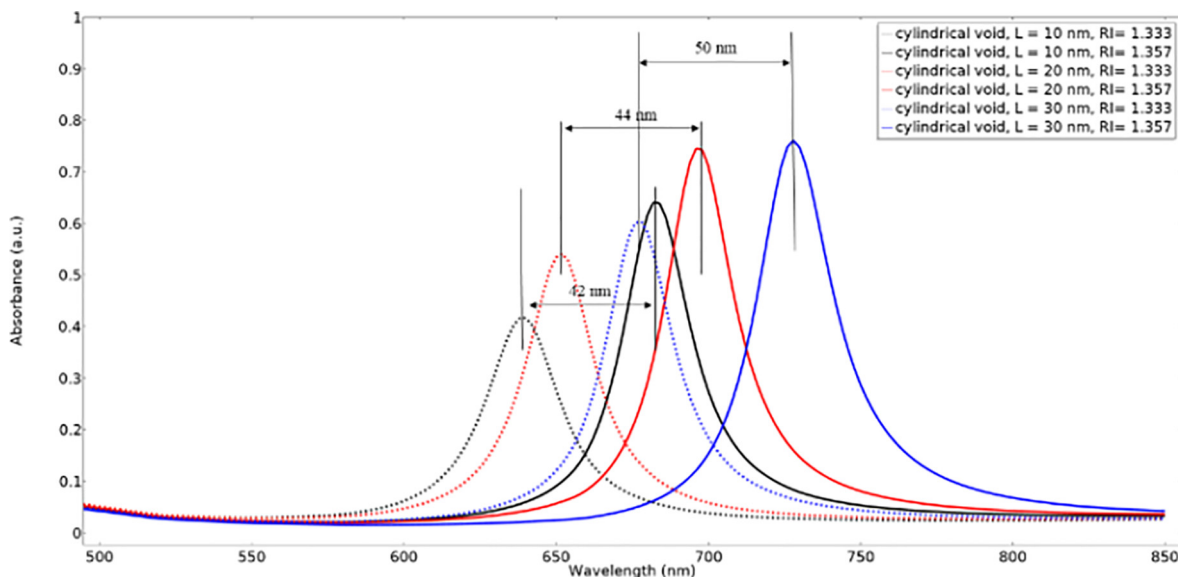


Fig. 3. The absorption spectra of the devices made from cylindrical nanovoid arrays with various depths of 10, 20 and 30 nm for the refractive indices of 1.333 (dotted lines) and 1.357 (solid lines).

30 nm) and “nanohole” is referred to the hole with a depth of 40 nm. The sensing characteristics of the devices were studied using two different materials with refractive indices of 1.333 and 1.357.

Absorption spectra of the modeled sensors are shown in Fig. 3, and as it is seen, the absorption peaks have higher intensity for all perforated thin films compared to that of the planar thin film. The absorbance increases as the depth of the cavity is increased, and it reaches the maximum value for the structure with 30 nm-nanovoids. The sensitivity values of  $1750 \frac{\text{nm}}{\text{RIU}}$ ,  $1830 \frac{\text{nm}}{\text{RIU}}$  and  $2083 \frac{\text{nm}}{\text{RIU}}$  were obtained for devices with nanovoid with depths of 10, 20, and 30 nm respectively.

The same study is performed for the sensor patterned with nanohole arrays, and the effect of the conformation of the hole (cylindrical and cubic) is further investigated. Fig. 4 shows the optical absorption spectra of the sensors made of a 40 nm thin film perforated with cubic holes (10 nm × 10 nm × 40 nm) or cylindrical holes (with a diameter of 10 nm) for two refractive indices of 1.333 and 1.357. According to the spectra, the sensitivity and accuracy of both sensors are approximately the same. The sensitivity of  $1916 \frac{\text{nm}}{\text{RIU}}$  for the sensors made of

cylindrical nanohole marginally improved to  $2000 \frac{\text{nm}}{\text{RIU}}$  for sensors with cubic nanoholes.

It would be interesting to compare the SPs field enhancement for both nanovoid and nanohole structures, at resonance condition. In this study, the electric field profiles of the structures, which showed the highest sensitivity are compared. Fig. 5a illustrates the electric field distribution of the 30 nm nanovoid-sensor. As one can see, a strong coupling between the evanescent wave and the SPP modes appears on the rim of the structures on the metal-dielectric interface.

The graph that shows the variation of the electric field intensity over a cut line along the z-axis is also presented in Fig. 5b. The inset of the figure shows the geometry of the device schematically and the position of the cut line considered in this study. By comparing the field intensity graph shown in Fig. 5b with that of the conventional SPR shown in Fig. 2c, it can be concluded that the device is supporting both SPR and LSPR modes. The first peak in Fig. 5b with lower intensity and higher decay length refers to SPR mode. The sharp peak at metal-dielectric interface with a higher intensity (about one order of magnitude) and a

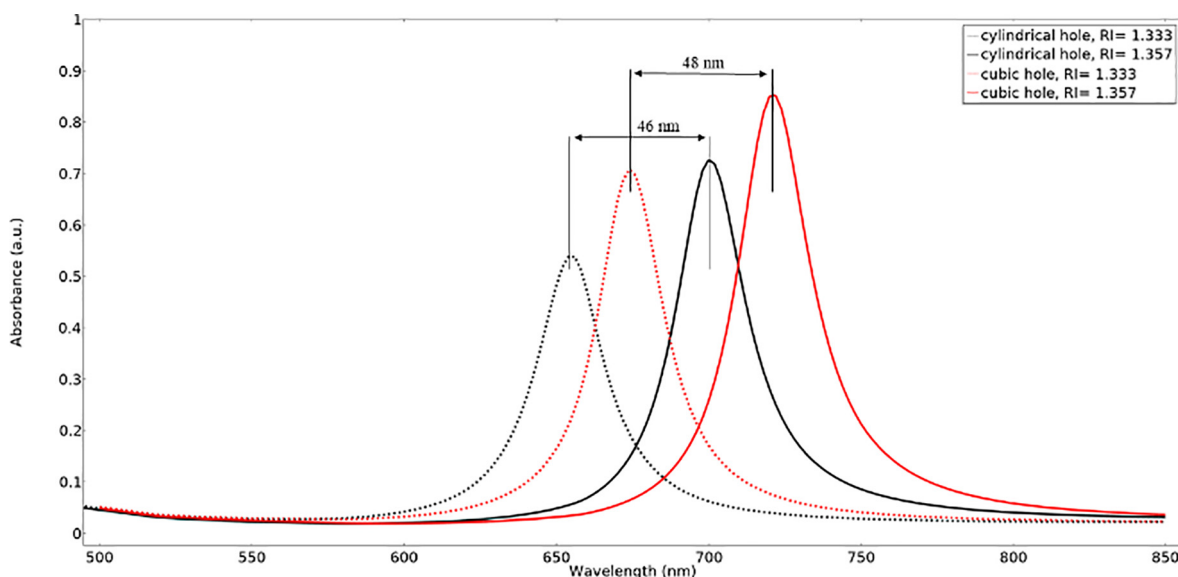
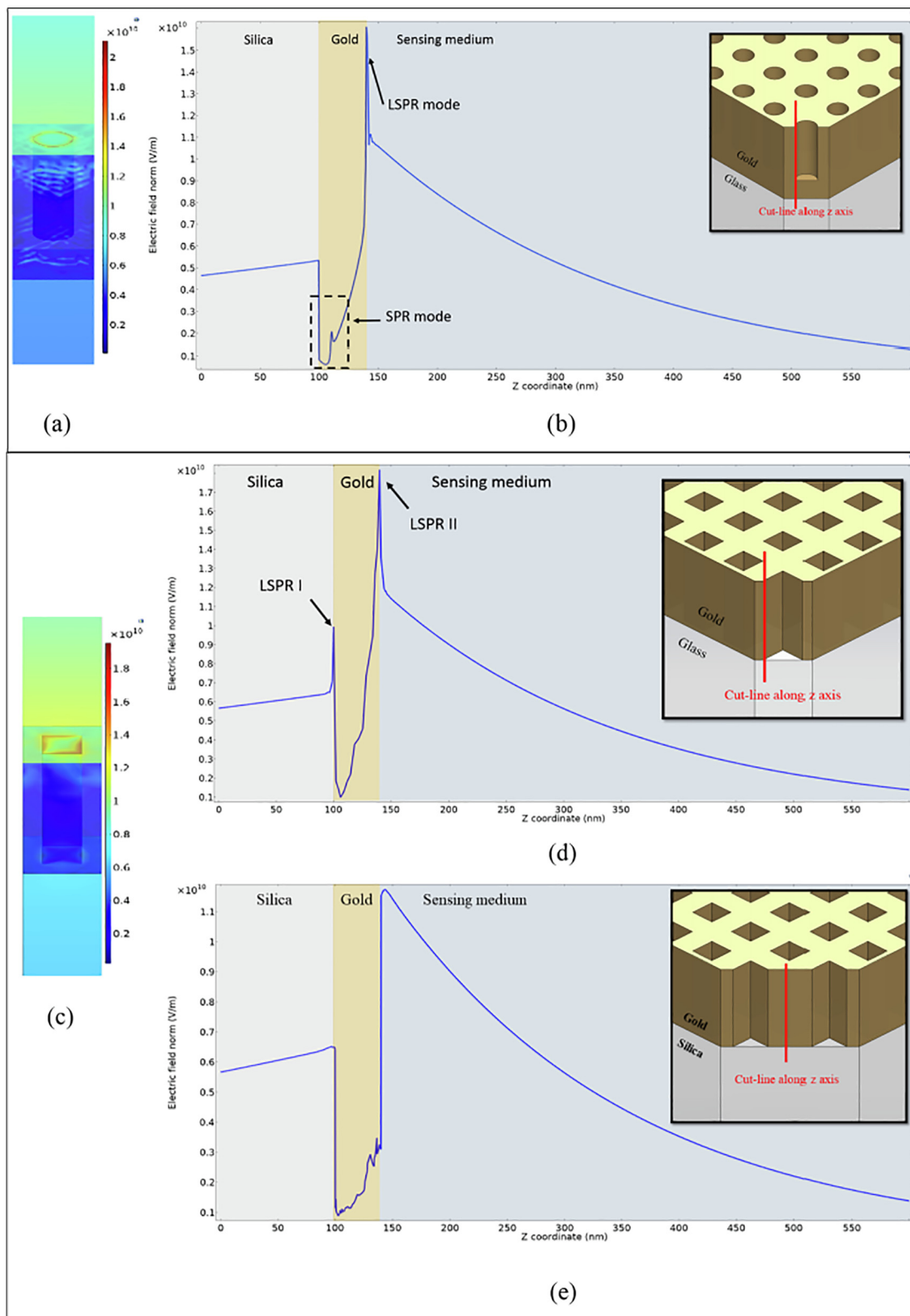


Fig. 4. The absorption spectra of the devices made from cubic/cylindrical nanohole arrays for two refractive indices of 1.333 (dotted lines) and 1.357 (solid lines).



**Fig. 5.** (a, b) The Electric field profile in 30 nm-nanovoid sensor at the resonance wavelength, (a) 3D unit cell (b) along a cut line as shown in the inset. (c–e) The Electric field profile in cubic nanohole-device at the resonance wavelength, (c) 3D unit cell, (d) along a cut line which passes through the film discontinuities (as shown in the inset), (e) along a cut line (as shown in the inset) through the thin film. By comparing the graphs shown in (d) and in (e), it can be observed that SPR occurs throughout the continues thin film, while LSPR occurs at film discontinuity boundaries with sharp edges.

very small decay length refers to the occurrence of LSPR in the sensor [34].

In the case of the sensors based on nanoholes, as can be seen in Fig. 5c, localization occurs at both upper and lower rims of the hole, which results in higher absorbance (Fig. 4) compared to what showed by devices with nanovoids (Fig. 3). Fig. 5d illustrates the field intensity graph along a cut line through the geometry. The position of the cut line is schematically shown in the inset. Two sharp peaks at silica-metal and metal-dielectric interfaces refer to the occurrence of LSPR in both lower and upper rims of the structure. By changing the position of the cut line in a way not to cut through the holes (Fig. 5e), the variation of the electric field shows only the SPR mode of the device. Observing the graphs shown in Fig. 5d and e confirms the occurrence of both LSPR and SPR modes in perforated thin films.

#### Protrusive thin films

The performance of the designed plasmonic sensor is studied for cylindrical/cubic protrusive features over a 40 nm thin film.

In this model array of nanowires is implemented above the 40 nm metallic thin film. The effect of the height of the nanowires (cylindrical or cubic conformations) was investigated by comparing the performance of the devices made of 10, 20, 30, and 40 nm nanowires. Using the same approach reported in sections A and B, the refractive index sensitivity of the designed sensors was studied for two materials with refractive indices of 1.333 and 1.357.

The absorption spectra of the sensors containing cylindrical nanowires of various lengths are shown in Fig. 6. As the figure shows the resonance wavelengths are shifted toward the infrared region, and this is more pronounced as the height of the nanowires is increased. According to FWHM of the absorption spectra the accuracy of the sensors is being decreased as the height of nanowires is increased. The same study was performed for the cubic nanowires, and detailed results of the models based on the absorption spectra of the sensors are presented in Table 1.

The results demonstrate higher sensitivity for the cylindrical nanowires compared to that of the cubic nanowires of the same height. Furthermore, increasing the height of the nanowires up to 30 nm increases the sensitivity of the sensors. Above this height, the sensitivity of the sensor showed a decreasing trend for both cylindrical and cubic geometries. The maximum sensitivity of  $4916 \frac{\text{nm}}{\text{RIU}}$  was observed for the device containing 30 nm cylindrical nanowire supported by the 40 nm

**Table 1**

Detailed results based on the absorption spectra.

| NW Geometry | NW height (nm) | Sensitivity ( $\frac{\text{nm}}{\text{RIU}}$ ) | FOM    | Absorbance (a.u.) |            |
|-------------|----------------|--|--------|-------------------|------------|
|             |                |  |        | RI = 1.333        | RI = 1.357 |
| Cylindrical | 10             | 2416   | 80.43  | 0.63              | 0.817      |
|             | 20             | 4750   | 111.45 | 0.949             | 0.708      |
|             | 30             | 4916   | 23.91  | 0.525             | 0.319      |
|             | 40             | 3583   | 8.84   | 0.3               | 0.212      |
| Cubic       | 10             | 2333   | 78.13  | 0.662             | 0.841      |
|             | 20             | 3291   | 85.17  | 0.96              | 0.797      |
|             | 30             | 4875   | 24.70  | 0.495             | 0.298      |
|             | 40             | 3416   | 8.78   | 0.275             | 0.194      |

thin film.

According to sensitivity and FOM of all models, the sensor with 20 nm cylindrical nanowires can be considered as the optimum design since both the sensitivity and accuracy are high for this device. Consequently, to narrow down our investigations, further studies are performed only on this model.

The distribution of the electric field at resonance condition for this model is shown in Fig. 7a. According to the figure, the electric field is enhanced around the nanowire rims. Fig. 7b and c show the plane view of electric field intensity on a cross-section of the unit cell at the upper (Fig. 7b) and lower (Fig. 7c) rims of the nanowires. As it is seen the field enhancement is stronger at upper rim compared to the lower rim.

Similar to the nanohole arrays discussed in section B, the implementation of a metallic nanowire array on a metallic thin film results in co-excitation of SPR and LSPR modes. Fig. 8 presents the electric field variation along a cut line through the modeled sensor geometry (the position of the cut line is shown in the inset of the figure). Considering the z-coordination of the geometry, the SPR peak is positioned at the bottom of the nanowire. By comparing the SPR peak of this device with that of the 40 nm planar thin film shown in Fig. 2c, one can notice that the electric field variation has a similar characteristic of the conventional SPR. The second peak is the LSPR characteristic of the device which results in such a sharp strong field enhancement with a few nm decay lengths.

Fig. 9 shows the calibration curve of the optimum device, which determines the sensing capability of the sensor. The curve shows the observed resonance wavelengths for various sensing mediums with

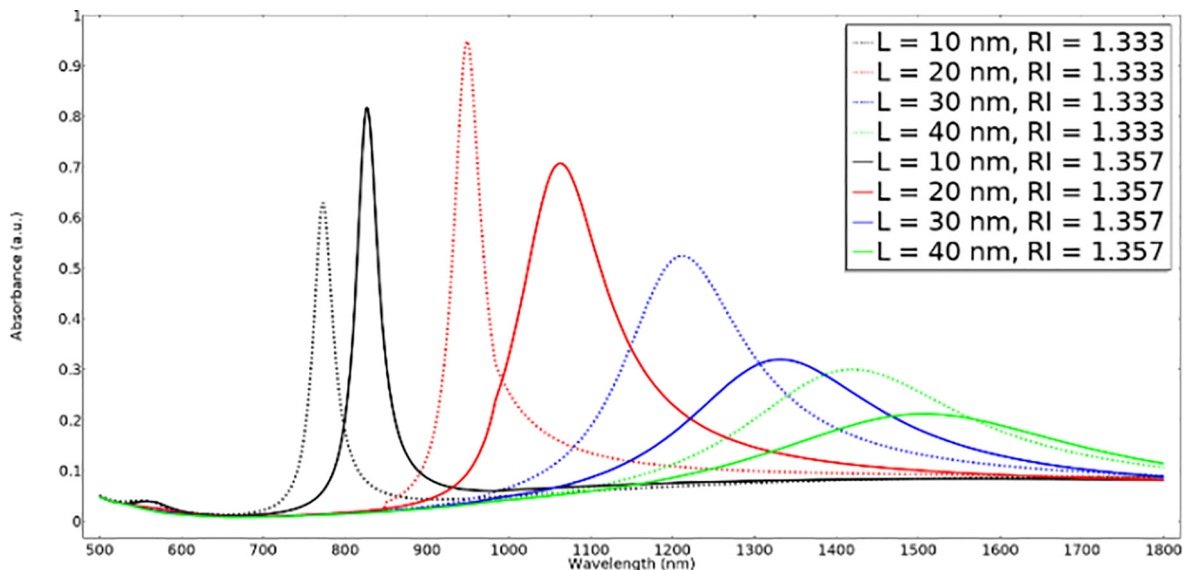


**Fig. 6.** Absorption spectra of the sensors made of nanowires with various lengths of 10, 20, 30 and 40 nm supported by 40 nm thin film for two materials with refractive indices of 1.333 and 1.357.

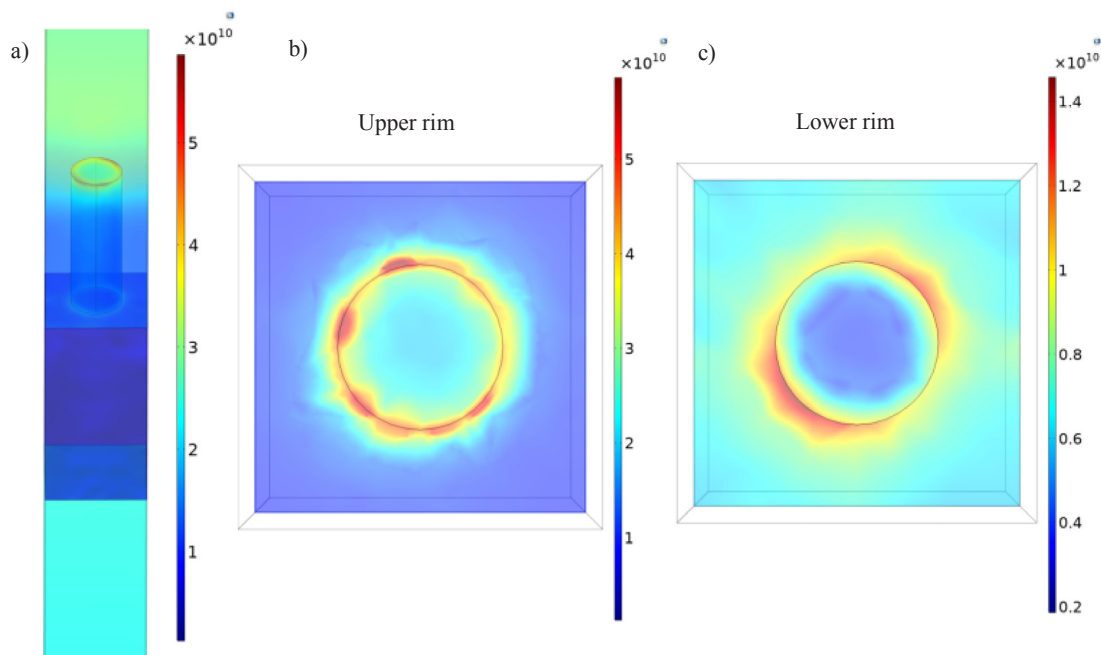


Fig. 7. Electric field distribution in a 20 nm-nanowire sensor over, (a) The unit cell, (b) Upper rim and (c) Lower rim.

known refractive indices. Selected substances are purified water, propane, water, ether, glycerol, acetone, acetic acid, and propyl with refractive indices of 1.333, 1.34, 1.346, 1.35, 1.357, 1.36, 1.37 and 1.38, respectively. A good linearity in the calibration curve is shown in the figure, which indicates the applicability of the sensor to identify the refractive indices of unknown mediums as a function of resonance wavelength. As can be observed the shift in the resonance wavelength is significantly enlarged as the refractive index of the surrounding medium increases. This results in higher sensitivity of the sensor for the mediums with higher refractive indices. The average sensitivity of the device is  $5847.2 \frac{\text{nm}}{\text{RIU}}$  which is calculated by the slope of a linear fit to the calibration data.

**Conclusions**

In this work, a refractive index sensor based on SPR and LSPR was modeled, and its performance was analyzed and simulated by the finite element method using COMSOL Multiphysics tool. The structure of the

sensor was made of a silica glass covered with layer of gold thin film and a dielectric material at the vicinity of the gold layer. The effect of thickness of the thin film and its patterned surface on the sensitivity and accuracy of the sensor was studied. Studies showed that in case of patterned metal thin film, the effect of both SPR and LSPR on the sensitivity of the device can be observed. The absorbance spectroscopy of the models demonstrated that the sensors made of 20 nm nanowires supported by 40 nm thin film gives us the optimum results in terms of sensitivity and FOM.

The device was used to measure the resonance wavelength for several substances with various refractive indices; the variation of resonance wavelength with respect to refractive indices was plotted. The results show a linear characteristic of the device, which may be able to be used to identify substances with unknown index of refraction.

To improve the achieved sensitivities in this research, further investigations can be done to study the effect of the size and periodicity of the patterned structures on the thin film.

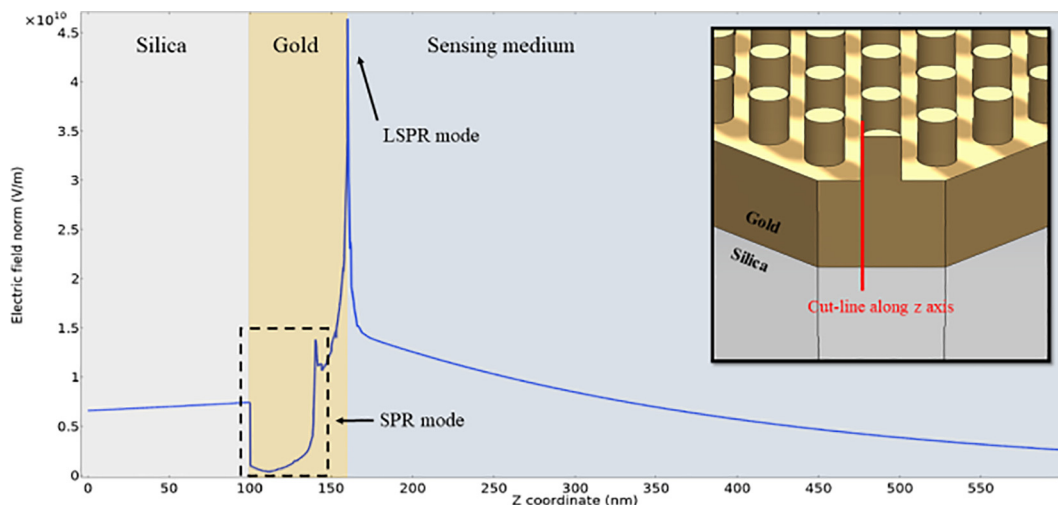


Fig. 8. The Electric field profile of the sensor made of 20 nm nanowires supported by 40 nm thin film at the resonance wavelength along a cut line as shown in the inset.

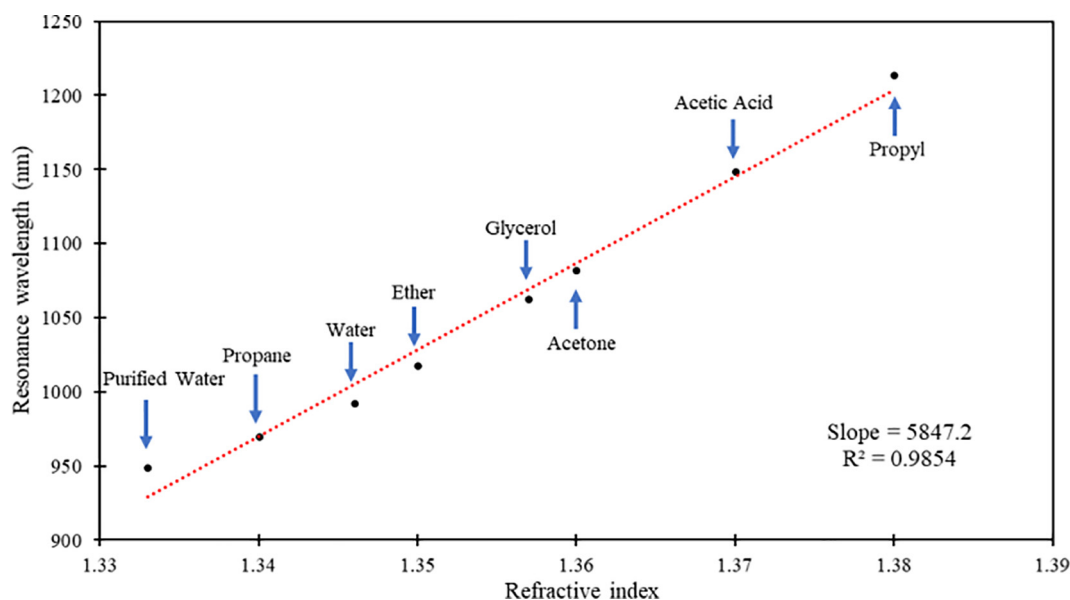


Fig. 9. The calibration curve of the resonance wavelengths as a function of refractive indices of selected substances. The linear line fitted our data with  $R^2$  of 0.9854. The average sensitivity of 5847.2 is calculated by the slope of the curve.

#### Author's statement

Armin Agharazy Dormeny, Parsoua Abedini Sohi, and Mojtaba Kahrizi: Writing and editing the manuscript.  
 Armin Agharazy Dormeny: Data acquisition.  
 Parsoua Abedini Sohi: Writing the manuscript.  
 Mojtaba Kahrizi: Supervision.

#### Declaration of Competing Interest

The authors declare that they have no known competing financial interests or personal relationships that could have appeared to influence the work reported in this paper.

#### Acknowledgments

The authors would like to acknowledge the support of the National Science and Engineering Research Council of Canada and Gina Cody School of Engineering and Computer Science at Concordia University.

#### References

- [1] Homola J. Surface plasmon resonance sensors for detection of chemical and biological species. *Chem Rev* 2008;108(2):462–93.
- [2] Kretschmann E, Raether H. Radiative decay of non radiative surface plasmons excited by light. *Z Naturforschung A* 1968;23(12):2135–6.
- [3] Otto A. Excitation of nonradiative surface plasma waves in silver by the method of frustrated total reflection. *Z Phys A Hadrons Nuclei* 1968;216(4):398–410.
- [4] Jorgenson R, Yee S. A fiber-optic chemical sensor based on surface plasmon resonance. *Sens Actuators B Chem* 1993;12(3):213–20.
- [5] Kawasaki D, et al. Core-shell-structured gold nanocone array for label-free DNA sensing. *ACS Appl Nano Mater* 2019.
- [6] McFarland AD, Van Duyne RP. Single silver nanoparticles as real-time optical sensors with zeptomole sensitivity. *Nano Lett* 2003;3(8):1057–62.
- [7] Gupta B, Shrivastav A, Usha S. Surface plasmon resonance-based fiber optic sensors utilizing molecular imprinting. *Sensors* 2016;16(9):1381.
- [8] Couture M, Zhao SS, Masson J. Modern surface plasmon resonance for bioanalytics and biophysics. *Phys Chem Chem Phys* 2013;15(27):11190–216.
- [9] Cennamo N, et al. Refractive index sensing through surface plasmon resonance in light-diffusing fibers. *Appl Sci* 2018;8(7):1172.
- [10] Liu K, et al. Theoretical modeling of a coupled plasmon waveguide resonance sensor based on multimode optical fiber. *Opt Commun* 2018;410:552–8.
- [11] Amendola V, et al. Surface plasmon resonance in gold nanoparticles: a review. *J Phys Condensed Matter* 2017;29(20):203002.
- [12] Long Y, Jing C. Localized surface plasmon resonance based nanobiosensors. 2014.
- [13] Live LS et al. Enhanced SPR sensing based on micropatterned thin films. In *Plasmonics in biology and medicine VIII*; 2011.
- [14] Willets KA, Van Duyne RP. Localized surface plasmon resonance spectroscopy and sensing. *Annu Rev Phys Chem* 2007;58:267–97.
- [15] Chen J, et al. Optical magnetic field enhancement by strong coupling in metamaterials. *J Lightwave Technol* 2018;36(13):2791–5.
- [16] Chen J, et al. Enhancing the magnetic plasmon resonance of three-dimensional optical metamaterials via strong coupling for high-sensitivity sensing. *J Lightwave Technol* 2018;36(16):3481–5.
- [17] Chen J, et al. Engineering the magnetic plasmon resonances of metamaterials for high-quality sensing. *Opt Express* 2017;25(4):3675–81.
- [18] Chen J, et al. Optical cavity-enhanced localized surface plasmon resonance for high-quality sensing. *IEEE Photon Technol Lett* 2018;30(8):728–31.
- [19] Liu P, et al. An ultra-low detection-limit optofluidic biosensor with integrated dual-channel Fabry-Pérot cavity. *Appl Phys Lett* 2013;102(16):163701.
- [20] Liu P, et al. An optofluidics biosensor consisted of high-finesse Fabry-Pérot resonator and micro-fluidic channel. *Appl Phys Lett* 2012;100(23):233705.
- [21] Maier SA. *Plasmonics: fundamentals and applications*. 2007.
- [22] Pang L, et al. Spectral sensitivity of two-dimensional nanohole array surface plasmon polariton resonance sensor. *Appl Phys Lett* 2007;91(12):123112.
- [23] Dolev I, Epstein I, Arie A. Surface-plasmon holographic beam shaping. *Phys Rev Lett* 2012;109(20):203903.
- [24] Kasap SO. *Optoelectronics and photonics: principles and practices*. 340.
- [25] Yakubovsky DI, et al. Optical constants and structural properties of thin gold films. *Opt Express* 2017;25(21):25574–87.
- [26] Raether H. *Surface plasmons on smooth surfaces and on gratings*. 1988.
- [27] Michel D, Xiao F, Alameh K. A compact, flexible fiber-optic surface plasmon resonance sensor with changeable sensor chips. *Sens Actuators B Chem* 2017;246:258–61.
- [28] Novotny L, Hecht B. *Principles of nano-optics*. 2012.
- [29] Yim S, et al. Transferrable plasmonic Au thin film containing sub-20 nm nanohole array constructed via high-resolution polymer self-assembly and nanotransfer printing. *ACS Appl Mater Interfaces* 2018;10(3):2216–23.
- [30] Suzuki H, et al. Effects of gold film thickness on spectrum profile and sensitivity of a multimode-optical-fiber SPR sensor. *Sens Actuators B Chem* 2008;132(1):26–33.
- [31] Iga M, Seki A, Watanabe K. Gold thickness dependence of SPR-based hetero-core structured optical fiber sensor. *Sens Actuators B Chem* 2005;106(1):363–8.
- [32] Sharma AK, Gupta B. On the performance of different bimetallic combinations in surface plasmon resonance based fiber optic sensors. *J Appl Phys* 2007;101(9):093111.
- [33] Kaminska I, et al. Near-field and far-field sensitivities of LSPR sensors. *J Phys Chem C* 2015;119(17):9470–6.
- [34] Read T, Olkhov RV, Shaw AM. Measurement of the localised plasmon penetration depth for gold nanoparticles using a non-invasive bio-stacking method. *Phys Chem Chem Phys* 2013;15(16):6122–7.